12. Roebroek, A. J. *et al.* Genomic organization of the human NSP gene, prototype of a novel gene family encoding reticulons. *Genomics* **32,** 191–199 (1996).
13. Roebroek, A. J., Contreras, B., Pauli, I. G. & Van de Ven, W. J. cDNA cloning, genomic organization, and expression of the human RTN2 gene, a member of a gene family encoding reticulons. *Genomics* **51,** 98–106 (1998).
14. Moreira, E. F., Jaworski, C. J. & Rodriguez, I. R. Cloning of a novel member of the reticulon gene family (RTN3): gene structure and chromosomal localization to 11q13. *Genomics* **58,** 73–81 (1999).
15. Morris, N. J., Ross, S. A., Neveu, J. M., Lane, W. S. & Lienhard, G. E. Cloning and characterization of a new member of the reticulon family. *Biochim. Biophys. Acta* **1450,** 68–76 (1991).
16. Jackson, M. R., Nilsson, T. & Peterson, P. A. Identification of a consensus motif for retention of transmembrane proteins in the endoplasmic reticulum. *EMBO J.* **9,** 3153–3162 (1991).
17. Senden, N. H. *et al.* Neuroendocrine-specific protein C (NSP-C): subcellular localization and differential expression in relation to NSP-A. *Eur. J. Cell Biol.* **69,** 197–213 (1996).
18. Bandtlow, C. E. & Loschinger, J. Developmental changes in neuronal responsiveness to the CNS myelin-associated neurite growth inhibitor NI-35/250. *Eur. J. Neurosci.* **9,** 2743–2752 (1997).
19. Takahashi, T., Nakamura, F., Jin, Z., Kalb, R. G. & Strittmatter, S. M. Semaphorin A and E act as antagonists of neuropilin-1 and agonists of neuropilin-2 receptors. *Nature Neurosci.* **1,** 487–493 (1998).
20. Takahashi, T. *et al.* Plexin-neuropilin1 complexes form functional semaphorin-3A receptors. *Cell* **99,** 59–69 (1999).
21. Goshima, Y., Nakamura, F., Strittmatter, P. & Strittmatter, S. M. Collapsin-induced growth cone collapse mediated by an intracellular protein related to *unc*-33. *Nature* **376,** 509–514 (1995).
22. Wang, L. H. & Strittmatter, S. M. A family of rat CRMP genes is differentially expressed in the nervous system. *J. Neurosci.* **16,** 6197–6207 (1996).
23. Jin, Z. & Strittmatter, S. M. Rac1 mediates collapsin-induced growth cone collapse. *J. Neurosci.* **17,** 6256–6263 (1997).
24. Strittmatter, S. M., Fishman, M. C. & Zhu, X. P. Activated mutants of the α subunit of G_o promote an increased number of neurites per cell. *J. Neurosci.* **14,** 2327–2338 (1994).
25. Vartanian, T., Fischbach, G. & Miller, R. Failure of spinal cord oligodendrocyte development in mice lacking neuregulin. *Proc. Natl Acad. Sci. USA* **96,** 731–735 (1999).

Acknowledgements

The authors thank A. Fournier for invaluable experimental advice and assistance. This work was supported by grants to S.M.S. from the NIH and the American Paralysis Association, and to F.N. from the Spinal Cord Research Fund of the Paralyzed Veterans of America. S.M.S. is an Investigator of the Patrick and Catherine Weldon Donaghue Medical Research Foundation.

Correspondence and requests for materials should be addressed to S.M.S. (e-mail: stephen.strittmatter@yale.edu).

Torque-generating units of the flagellar motor of *Escherichia coli* have a high duty ratio

William S. Ryu*, Richard M. Berry† & Howard C. Berg*

* *Department of Molecular and Cellular Biology, Harvard University, 16 Divinity Avenue, Cambridge, Massachusetts 02138, USA and Rowland Institute for Science, 100 Edwin H. Land Boulevard, Cambridge, Massachusetts 02142, USA*
† *The Randall Centre, King's College London, London SE1 1UL, UK*

Rotation of the bacterial flagellar motor is driven by an ensemble of torque-generating units containing the proteins MotA and MotB[1–3]. Here, by inducing expression of MotA in *motA*$^-$ cells under conditions of low viscous load, we show that the limiting speed of the motor is independent of the number of units: at vanishing load, one unit turns the motor as rapidly as many. This result indicates that each unit may remain attached to the rotor for most of its mechanochemical cycle, that is, that it has a high duty ratio[4]. Thus, torque generators behave more like kinesin, the protein that moves vesicles along microtubules, than myosin, the protein that powers muscle. However, their translation rates, stepping frequencies and power outputs are much higher, being greater than 30 μm s^{-1}, 12 kHz and 1.5 × 10^5 pN nm s^{-1}, respectively.

Bacterial flagellar motors are driven by a transmembrane ion flux (reviewed in refs 5, 6). Most studies of their physiology have been done at low speeds, characteristic of high viscous loads, where translation rates of ions or movement of internal mechanical components are not limiting. To study their behaviour at higher speeds, we developed a new motor assay (Fig. 1a, inset). Instead of tethering a cell to a glass surface by a single flagellum and watching the cell body spin[7], we fixed the cell body to the glass surface and attached a polystyrene bead to a stub of one of its flagellar filaments. By using beads of various sizes (0.3–1 μm diameter), we could vary the load by a factor of more than 10. The bead was followed in a weak optical trap by back focal plane interferometry[8].

Figure 1a, b shows speed records for cells under high and low load, respectively. Upon induction of MotA expression, discrete increments in speed were observed. At high load (Fig. 1a), the increase in speed was linear with the torque-generator number, *N*, as observed previously with tethered cells[1,2]. However, at lower load (Fig. 1b), the speed tended to saturate at high torque-generator numbers. The data for different bead sizes are summarized in Fig. 2a. In Fig. 3a we show torque–speed curves for motors with between one and five torque-generating units, constructed from the data of Fig. 2a. At low speeds, the torque produced by a motor with *N* generators is simply *N* times the torque produced by a motor with one generator. At high speeds, the torques decline, and the curves are consistent with a limiting speed at zero torque of about 300 Hz.

The behaviour of the motor can be understood in terms of the 'duty ratio' of the torque generators[4], where the duty ratio, *D*, is defined as the fraction of time for which a generator is bound to the rotor. As the motor works against a viscous load, speed is proportional to the applied torque. At high loads, speed increases linearly with *N* whether *D* is small (close to 0) or large (close to 1). If *D* is small, the torque-generating units work independently of one another, because the probability that two might be attached at the same time is small; speed is proportional to the time-averaged torque. If *D* is large, each unit has time to reach thermodynamic equilibrium and exert the same torque; speed is proportional to the total torque. At vanishing load, speed increases linearly with *N* when

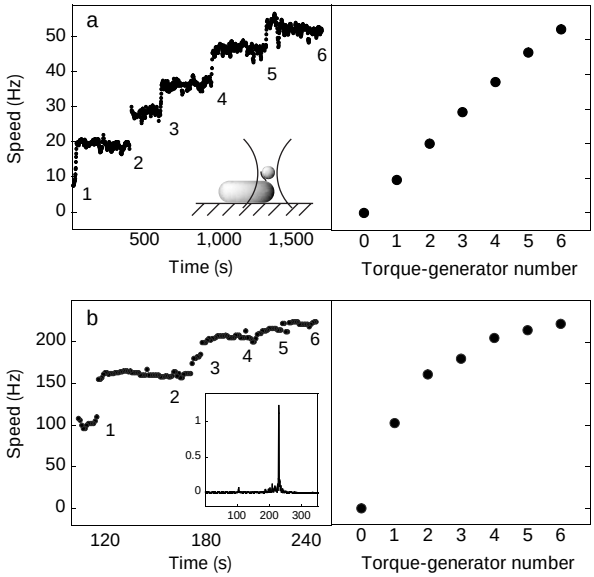

Figure 1 Measurements made at high and low load. **a**, Induction of torque in a motor driving a bead of 1.03 μm diameter (left). Speed is shown as a function of time, and the number of torque generators is indicated. Inset, a small bead attached to a segment of a flagellar filament and followed in a weak optical trap. Right, mean speed as a function of torque-generator number. Error bars are smaller than data markers. **b**, As in **a** for a different motor driving a bead of 0.30 μm diameter. Inset, the power spectrum of the signal from 80 revolutions of a 0.36-μm bead. The abscissa is frequency (Hz), and the ordinate is power (arbitrary units).

D is small but not when D is large. If D is small, the torque-generating units work independently of one another, as before, and again speed is proportional to the time-averaged torque. If D is large, on the other hand, any unit bound to the rotor limits its speed. Assuming that the time required for a unit to complete a mechano-chemical cycle is independent of the torque exerted by other units, the speed is determined by the displacement per cycle divided by the cycle time. So our data are consistent with a model in which the duty ratio is close to 1.

Our results can be reproduced by a model (Box 1) in which $D = 1$ and the rate constants for forward transitions are load independent, as shown in Figs 2b and 3b. If an unbound state is introduced ($D < 1$) or if all forward rate constants are load-dependent, the zero-load speeds vary with N (Box Fig. b) and the concave-down shape of the torque-speed curves[9,10] cannot be reproduced. Our data do not rule out zero-load speeds that vary with N, as it was not possible to measure these speeds directly—beads had to be at least 0.30 μm in diameter to detect rotation. By extrapolating the curves for $N = 3, 4$ and 5 unit motors to zero torque (using the fastest three data points of each curve, Fig. 3a), we estimate the zero-load speeds to be 306 ± 76 Hz, 299 ± 47 Hz and 305 ± 35 Hz, respectively. Combining these values we obtain 303 ± 32 Hz. The ratio of the lowest to the highest zero-load speeds within the error limits is ~0.8. When this ratio is compared to the corresponding ratios of zero-load speeds obtained from simulations at various duty ratios (Box Fig. b), we find $D > 0.6$.

We conclude that the torque-generating units remain attached to the rotor most of the time; in other words, that their duty ratio is greater than 0.6 and more likely to be closer to 1. The speed might saturate at low loads at a lower duty ratio if the generators work cooperatively at low loads and bind synchronously; however, there is at present no evidence for cooperative interactions between units. Alternatively, a unit that appears to have a duty ratio close to 1 might be composed of more than one interacting subunit with a lower duty ratio, as in the dimeric kinesin molecule. If so, our analysis applies to the composite structure, not the individual subunits.

It has been found from fluctuation analysis of tethered cells rotating at low speed that the total number of steps taken by the rotor per revolution is proportional to torque-generator number, N (ref. 3). This implies that the rotor step size decreases with N. This could be understood if, on stepping along the periphery of the rotor a fixed distance d, the Nth torque-generating unit had to work with the other $N - 1$, suggesting a high duty ratio. Our work supports this argument and shows that the duty ratio remains high for speeds up to a few hundred hertz. Thus, torque generators behave more like kinesin than myosin. Single kinesin molecules take hundreds of steps along a microtubule without falling off[11], whereas myosin spends most of its mechanochemical cycle detached from the actin filament, binding only briefly to undergo a force-producing step[12]. In both cases, the function of the motor molecule dictates the duty ratio. When vesicles are moved along microtubules, procession is more important than speed, so kinesin has a high duty ratio. When muscles contract, speed is more important than procession, so many myosins work together, each with a low duty ratio[13]. Evidently, for the flagellar motor, the ability to drive sizeable viscous loads at high speeds requires that the torque generators work with a high duty ratio. For *E. coli*, this probably relates to the forces required to form or disrupt flagellar bundles, processes essential for chemotaxis[14]. However, a high duty ratio requires that each generator completes a fixed number of torque-generating cycles each revolution, regardless of speed, so high speeds require high

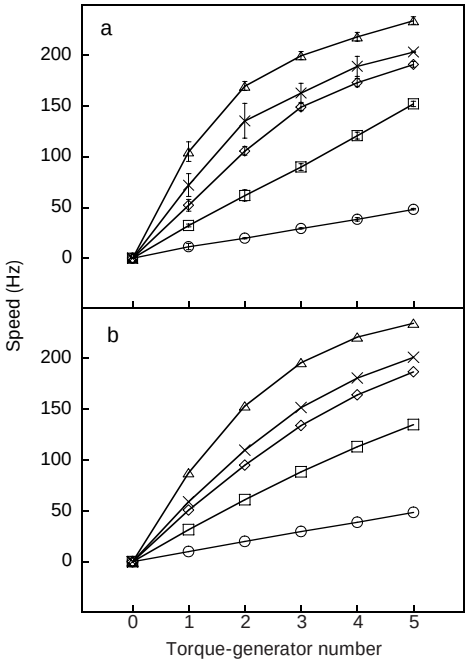

Figure 2 Speeds, measured and simulated. **a**, Speed as a function of torque-generator number for different bead sizes. Reading from top to bottom, the diameter of the beads in micrometres (and the numbers of motors assayed at each bead size) were 0.30 (12), 0.356 (15), 0.41 (8), 0.535 (11) and 1.03 (3), respectively. The data points and error bars are the means and standard deviations over the cell ensemble, with the mean speeds for each torque-generator number weighted equally. **b**, A Monte-Carlo simulation of the behaviour of a motor shown as a function of torque-generator number, N. Reading from top to bottom, the viscous drag coefficients were 2.7, 4.3, 5.1, 8.5 and 28.0 pN nm per revolution per s.

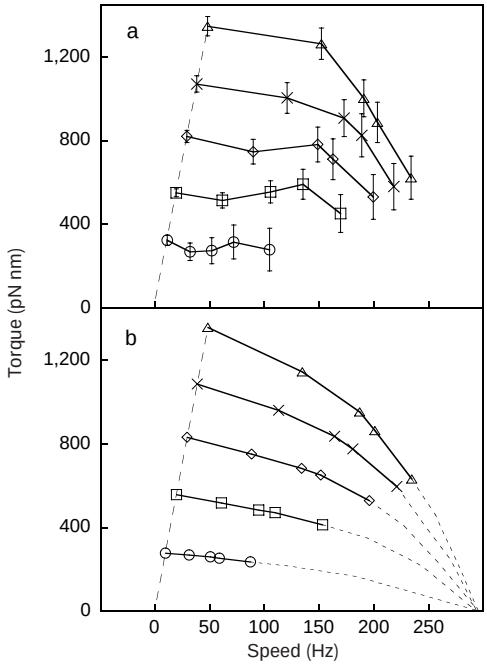

Figure 3 Torques, measured and simulated. **a**, Torque–speed curves for motors with 1 (bottom) to 5 (top) torque-generating units. The curves were derived from the data of Fig. 2a, as described in Methods. The points for a given bead size fall on a line—one such line is shown—whose slope is equal to the viscous drag coefficient. Reading from left to right, the viscous loads were 27.8, 8.5, 5.3, 4.4 and 2.7 pN nm per revolution per s. **b**, A similar plot derived from the simulation of Fig. 2b, including points computed at lower viscous loads (dashed lines).

Box 1

Flagellar motor model

A model was developed to reproduce the torque–speed curves, which are concave downwards[9,10]. Torque generators work independently with a three-state cycle, $E_p \leftrightarrow A_p \leftrightarrow B_p \leftrightarrow E_{p+1}$, where p identifies the binding site[28]. Each cycle carries one proton across the membrane and moves the equilibrium position of the rotor by $\varphi = 2\pi/n_r$, where n_r is the number of binding sites. Proton exchange with the external and internal media is represented by transitions $E_p \leftrightarrow A_p$ and $B_p \leftrightarrow E_{p+1}$, respectively, and changes that occur while protons are in the motor are represented by the transition $A_p \leftrightarrow B_p$. For each state ($i = E_p, A_p, B_p$) the energy $U_i(\theta)$ represents the elastic, electrostatic, and/or hydrophobic energies involved in generator/rotor interaction. Each proton provides the energy $U_H = qV_m$, where q is the proton charge and V_m the protonmotive force, 150 mV. Rate constants for forwards and backwards transitions are given by $k_{ij} = k^0\exp(\lambda\Delta G_{ij}/k_bT)$ and $k_{ji} = k^0\exp[(\lambda - 1)\Delta G_{ij}/k_bT]$, respectively. $\Delta G_{ij} = U_i(\theta) - U_j(\theta) + \alpha_{ij}U_H$, where α_{ij} is the fraction of U_H dissipated in the transition, λ varies from 0 to 1 and specifies how much changes in ΔG affect forward as opposed to backward rate constants, k^0 controls the intrinsic rate of the transition, k_b is Boltzmann's constant and T is the absolute temperature. Each unit exerts a torque $T = -dU_i/d\theta$, and the total motor torque is the sum over all units. Transitions between states and the stochastic equations for rotation of the rotor and bead attached via an elastic link (proximal hook stiffness, $k_\theta = 400$ pN nm per radian)[29,30] are modelled by Monte-Carlo simulation.

The following model parameters were necessary to reproduce the measured torque–speed curves[9,10]. A powerstroke mechanism was chosen, with 90% of U_H and 90% of φ placed in the transition $A \leftrightarrow B$[28]. The rest of U_H and φ was split evenly between the other transitions. λ were all zero and k^0 were $1.23 \times 10^5\ s^{-1}$. Energy profiles, $U_i(\theta)$, for all three states were those of a spring that becomes less stiff at large extensions. That is, for positive extensions, ψ, the torque was given by

$$-\frac{dU}{d\theta} = \begin{cases} -\kappa_1\psi & : \psi < a \\ -[\kappa_1 a + \kappa_2(\psi - a)] & : \psi > a \end{cases}$$

where $\kappa_2 < \kappa_1$. For negative extensions (extensions that tend to slow the motor) the torque had the opposite sign. The predictions of the model were not very sensitive to the values of κ_1, κ_2 and a.

An example of a transition is shown in the energy diagram, a. A torque-generating unit in state A_p is in mechanical equilibrium with the rotor at 1. A forward transition to state B_p moves the equilibrium position through an angle ϕ_2, placing the unit out of mechanical equilibrium at 2. Torque $T = -dU_B(\theta)/d\theta$ is produced in the forward direction, until equilibrium is reached at 3. An earlier transition from state E_p to A_p moved the equilibrium position an angle ϕ_1. The next transition to state E_{p+1} will move the equilibrium position through an angle ϕ_3 to the next binding site $p + 1$, completing the cycle.

For simulations with $D < 1$, an unbound state that produced zero torque was introduced by setting $U_E(\theta)$ to be constant, and the rates into and out of this state were controlled by choosing the value of U_E. When the torque-generating units are unbound, the rotor can diffuse freely and respond to external torques, so the rotational drag coefficient of the rotor becomes important. When torque is exerted by the motor on the external load (bead), the tether winds up. When the units are unbound, the tether unwinds and moves the rotor backwards, implying a loss of efficiency. This happens because the viscous drag of the bead is much larger than that of the rotor. The rotational drag of the rotor was estimated to be $f_r = 0.25$ pN nm per (rev per s), modelled as a 50 nm diameter sphere in a lipid of viscosity 100 cp, yielding a relaxation time $\tau_r = f_r/k_\theta \approx 1$ ms.

Figure b shows the dependence of speed on the number of torque-generating units at zero load for different simulation parameters. The speeds have been normalized individually for each curve by the speed at $N = 5$; therefore, comparisons of speed cannot be made between curves. For units with $D = 1$ (squares), the zero-load speed is independent of N. For units with $D < 1$, the zero-load speed depends on N (circles, $D = 0.6$; triangles, $D = 0.23$). For units with load-dependent forward rate constants (diamonds, $D = 1$, $\lambda = 0.5$ and U_H and φ split equally between all three transitions), the zero-load speed also depends on N, irrespective of the duty ratio.

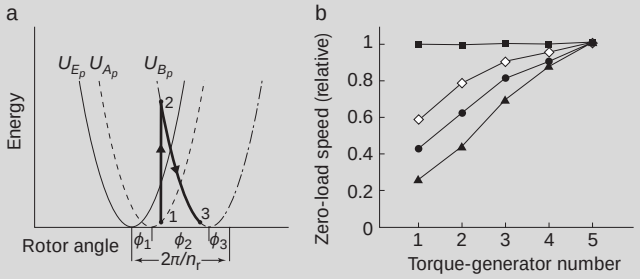

turnover rates. For example, a motor with $N = 5$ can spin a 0.30-μm bead at 240 Hz (Fig. 2a). If each unit steps 50 times per revolution—this is a lower bound[3]—the cycle frequency is at least 12 kHz. As the rotor is about 50 nm in diameter[15], the speed at the periphery exceeds 35 μm s^{-1}. Each unit can produce more than 5 pN of force and more than 1.75×10^5 pN nm s^{-1} of power. The Na^+-driven flagellar motor in *Vibrio alginolyticus* rotates even more rapidly (1,000 Hz), indicating that higher turnover rates and power outputs may be possible[16]. In comparison, a single kinesin molecule at saturating ATP concentration produces over 70 times less power, moving at about 0.5 μm s^{-1} while exerting a force of 5 pN (ref. 17). A single myosin molecule produces over 400 times less power, stepping 20 nm at a turnover rate of 10 s^{-1}, and exerting an average force of 2 pN (ref. 18). F_1-ATPase produces over 450 times less power, rotating at about 2 Hz against a load torque of 30 pN nm (ref. 19). The reason for the higher numbers in *E. coli* might be because the flagellar motor is driven by translocation of ions rather than binding, hydrolysis and release of nucleotides. □

Methods

Cells and beads

We used strain HCB1271. It was constructed from strain MS5037 (ref. 20), containing *motA*448 (ref. 21). MS5037 was made pil-minus by P1 transduction of pilA′-kan from strain HCB758 (refs 22, 23) and filament-minus by transduction of *fliC*::Tn*10* from strain C600 *hsm hsr fliC*::Tn*10* (ref. 24) by selection with the appropriate antibodies. We introduced MotA resurrection capability by transformation with pDFB36, carrying wild-type *motA* under an inducible promoter[2]. The *fliC*st (sticky filament) allele[25] was cloned into a plasmid compatible with pDFB36. Wild-type MotA was induced on addition of isopropyl β-D-thiogalactopyranoside (IPTG), and the sticky filaments readily adsorbed polystyrene beads. Reconstituted motors spun alternately clockwise and counterclockwise, but only the latter intervals were used here. Cells were prepared as described[9], but we sheared more completely by 60 passages through the shearing apparatus and resuspended at half the original volume in motility medium (10 mM potassium phosphate, pH 7.0, 0.1 mM EDTA). The cells were allowed to settle on a glass coverslip that had been treated with 4-aminobutyldimethoxy silane[9]. After 15 min, unattached cells were washed away, and a suspension of polystyrene beads was added (0.083% w/w in motility medium; 1.03, 0.525, 0.356 or 0.30 μm diameter, from Polysciences, or 0.41 μm diameter from Bangs Laboratories). After 5 min, unattached beads were washed away and the tethering medium was supplemented with tryptone broth (1% tryptone, Difco; 0.5% NaCl) at a concentration up to 20% v/v and with IPTG (final concentration 0.5 μM to 2.5 mM).

Data acquisition and analysis

The optical trap is described elsewhere[26]. We used two functionally identical instruments, one with a 980-nm MOPA laser[26] and the other with a 830-nm diode laser (Melles Griot). The power level at the back focal plane of the objective was 20 mW (980 nm, a wavelength at which the objective had a low transmittance) and <10 mW (830 nm). Trapping forces were too small to perturb the motion. Signals were sampled at 0.5–1 kHz and anti-alias filtered at 250 Hz. Power spectra were computed for successive 1-s blocks of data, and the speed–time plots were smoothed with a median filter of rank 4, which preserved discontinuities in the data. Decisions on the correspondence between speed and torque-

generator number were made at speeds below 160 Hz, where speed increased linearly with generator number.

Construction of torque-speed plots

We calculated torque, T, from estimates of drag coefficients, f, and measurements of speed. Rotational drag caused by an eccentrically rotating bead (of radius r_b rotating with an eccentricity r_e) attached to a flagellar stub (modelled as a thin prolate ellipsoid with a major radius a and minor radius b (10 nm) moving edge-on at a radius r_f) was estimated to be $8\pi\eta(r_b^3 + r_f^2 s) + 6\pi\eta r_e^2 r_b$ where s is the structural factor $a/[\ln(2a/b) + 0.5]$ (ref. 27). From digitized video images, the average eccentricity of rotation was 0.15 ± 0.5 μm. The rotational radius of the flagellar stub, r_f, which is proportional to stub length, was set to $a/2$. The average flagellar stub length, $2a$, was unknown and was left as a free parameter for subsequent fitting. The drag for each bead size was adjusted so that the data points for $N = 5$ generators coincided with a wild-type ($N = 8$) torque–speed curve[9,10], scaled to 5/8 the stall torque, but with the same knee and zero-torque speeds. The resulting torque–speed curves are shown in Fig. 3a. The fitted flagellar stub lengths were 1.22, 1.07, 0.95, 0.91 and 0.75 μm, for bead sizes 1.0, 0.54, 0.41, 0.36 and 0.30 μm, respectively.

Received 6 July; accepted 22 November 1999.

1. Block, S. M. & Berg, H. C. Successive incorporation of force-generating units in the bacterial rotary motor. *Nature* **309,** 470–473 (1984).
2. Blair, D. F. & Berg, H. C. Restoration of torque in defective flagellar motors. *Science* **242,** 1678–1681 (1988).
3. Samuel, A. D. T. & Berg, H. C. Torque-generating units of the bacterial flagellar motor step independently. *Biophys. J.* **71,** 918–923 (1996).
4. Leibler, S. & Huse, D. A. Porters versus rowers: a unified stochastic model of motor proteins. *J. Cell Biol.* **121,** 1357–1368 (1993).
5. Macnab, R. M. in *Escherichia coli and Salmonella: Cellular and Molecular Biology* Vol. 1 (eds Neidhardt, F. C. *et al.*) 123–145 (American Society for Microbiology, Washington, 1996).
6. Berry, R. M. & Armitage, J. P. The bacterial flagellar motor. *Adv. Microb. Physiol.* **41,** 291–337 (1999).
7. Silverman, M. & Simon, M. Flagellar rotation and the mechanism of bacterial motility. *Nature* **249,** 73–74 (1974).
8. Gittes, F. & Schmidt, C. F. Interference model for back-focal-plane displacement detection in optical tweezers. *Opt. Lett.* **23,** 7–9 (1998).
9. Berg, H. C. & Turner, L. Torque generated by the flagellar motor of *Escherichia coli*. *Biophys. J.* **65,** 2201–2216 (1993).
10. Chen, X. & Berg, H. C. Torque-speed relationship of the flagellar rotary motor of *Escherichia coli*. *Biophys. J.* (in the press).
11. Block, S. M., Goldstein, L. S. B. & Schnapp, B. J. Bead movement by single kinesin molecules studied with optical tweezers. *Nature* **348,** 348–352 (1990).
12. Uyeda, T., Abramson, P. D. & Spudich, J. A. The neck region of the myosin motor domain acts as a lever arm to generate movement. *Proc. Natl Acad. Sci. USA* **93,** 4459–4464 (1996).
13. Howard, J. Molecular motors: structural adaptations to cellular functions. *Nature* **389,** 561–567 (1997).
14. Macnab, R. M. Bacterial flagella rotating in bundles: a study in helical geometry. *Proc. Natl Acad. Sci. USA* **74,** 221–225 (1997).
15. DeRosier, D. J. The turn of the screw: the bacterial flagellar motor. *Cell* **93,** 17–20 (1998).
16. Muramoto, K. *et al.* High-speed rotation and speed stability of the sodium-driven flagellar motor in *Vibrio alginolyticus*. *J. Mol. Biol.* **251,** 50–58 (1995).
17. Visscher, K., Schnitzer, M. J. & Block, S. M. Single kinesin molecules studied with a molecular force clamp. *Nature* **400,** 184–189 (1999).
18. Toyoshima, Y. Y. *et al.* Myosin subfragment-1 is sufficient to move actin filaments *in vitro*. *Nature* **328,** 536–539 (1987).
19. Yasuda, R., Noji, H., Kinosita, K. J. & Yoshida, M. F_1-ATPase is a highly efficient molecular motor that rotates with discrete 120° steps. *Cell* **93,** 1117–1124 (1998).
20. Silverman, M. & Simon, M. Operon controlling motility and chemotaxis in *E. coli*. *Nature* **264,** 577–580 (1976).
21. Armstrong, J. B. & Adler, J. Genetics of motility in *Escherichia coli*: complementation of paralyzed mutants. *Genetics* **56,** 363–373 (1967).
22. Fung, D. C. Y. K. *Powering the* Escherichia coli *Flagellar Motor with an External Voltage Source*. Thesis, Harvard Univ. (1994).
23. Maurer, L. & Orndorff, P. E. Identification and characterization of genes determining receptor binding and pilus length of *Escherichia coli* type 1 pili. *J. Bacteriol.* **169,** 640–645 (1987).
24. Kuwajima, G. Flagellin domain that affects H antigenicity of *Escherichia coli* K-12. *J. Bacteriol.* **170,** 485–488 (1988).
25. Scharf, B. E., Fahrner, K. A., Turner, L. & Berg, H. C. Control of direction of flagellar rotation in bacterial chemotaxis. *Proc. Natl Acad. Sci. USA* **95,** 201–206 (1998).
26. Berry, R. M. & Berg, H. C. Absence of a barrier to backwards rotation of the bacterial flagellar motor demonstrated with optical tweezers. *Proc. Natl Acad. Sci. USA* **94,** 14433–14437 (1997).
27. Happel, J. & Brenner, H. *Low Reynolds Number Hydrodynamics* (Kluwer Academic, Drodrecht, 1991).
28. Berry, R. M. & Berg, H. C. Torque generated by the flagellar motor of *Escherichia coli* while driven backward. *Biophys. J.* **76,** 580–587 (1999).
29. Block, S. M., Blair, D. F. & Berg, H. C. Compliance of bacterial flagella measured with optical tweezers. *Nature* **338,** 514–517 (1989).
30. Block, S. M., Blair, D. F. & Berg, H. C. Compliance of bacterial polyhooks measured with optical tweezers. *Cytometry* **12,** 492–496 (1991).

Acknowledgements

We thank K. Fahrner and A. Samuel for plasmid and strain constructions, and K. Fahrner, A. Samuel and L. Turner for comments on the manuscript. This work was supported by the Wellcome Trust, the Rowland Institute for Science and by the US NIH.

Correspondence and requests for materials should be addressed to H.C.B.

The DExH protein NPH-II is a processive and directional motor for unwinding RNA

Eckhard Jankowsky*, Christian H. Gross†, Stewart Shuman† & Anna Marie Pyle*‡

* *The Department of Biochemistry and Molecular Biophysics, Columbia University, 630 W. 168th St, New York, New York 10032, USA*
† *The Program in Molecular Biology, Sloan-Kettering Institute,*
‡ *The Howard Hughes Medical Institute 1275 York Ave., New York, New York 10021, USA*

All aspects of cellular RNA metabolism and processing involve DExH/D proteins, which are a family of enzymes that unwind or manipulate RNA in an ATP-dependent fashion[1]. DExH/D proteins are also essential for the replication of many viruses, and therefore provide targets for the development of therapeutics[2]. All DExH/D proteins characterized to date hydrolyse nucleoside triphosphates and, in most cases, this activity is stimulated by the addition of RNA or DNA[1]. Several members of the family unwind RNA duplexes in an NTP-dependent fashion *in vitro*[1,3]; therefore it has been proposed that DExH/D proteins couple NTP hydrolysis to RNA conformational change in complex macromolecular assemblies[4]. Despite the central role of DExH/D proteins, their mechanism of RNA helicase activity remains unknown. Here we show that the DExH protein NPH-II unwinds RNA duplexes in a processive, unidirectional fashion with a step size of roughly one-half helix turn. We show that there is a quantitative connection between ATP utilization and helicase processivity, thereby providing direct evidence that DExH/D proteins can function as molecular motors on RNA.

Establishing a basic functional model for RNA helicase behaviour involved answering three fundamental questions: first, does the helicase unwind RNA in distinct, sequential steps? Second, does the enzyme dissociate from the RNA after each unwinding step or does it stay bound; that is, is the helicase processive? Third, does the helicase move from one defined point on its helical substrate to another defined point; is unwinding unidirectional?

We subjected the DExH helicase NPH-II from vaccinia virus[5] to quantitative kinetic analysis of RNA helicase activity using a collection of duplex RNA substrates that varied in composition and length. Kinetics of unwinding were monitored using gel-shift electrophoresis and fluorescence energy transfer methodologies. The RNA substrates contained a single-strand 3′ overhang, which is required for NPH-II unwinding activity[6]. The single-strand 3′ overhang was identical in length and sequence for every substrate (Fig. 1). Unwinding reactions were performed under single-turnover conditions with respect to the RNA substrate. A large excess of nonspecific 'trap RNA' was added to prevent helicase from re-associating with duplex once it falls off during the course of reaction.

In the absence of trap RNA, the unwinding rate and reaction amplitude (defined as the final fraction of unwound RNA) were both insensitive to duplex length (Fig. 1). Each reaction was first-order with a rate constant of $3.5 \pm 0.2\ \mathrm{min}^{-1}$ (Fig. 1). In the presence of trap RNA, the rates remained independent of duplex length; however, the reaction amplitude decreased with increasing duplex length (Fig. 1). These observations provide three mechanistic insights. First, the fact that long duplexes can be unwound at all in the presence of trap RNA provides strong qualitative evidence that the helicase is a processive enzyme, consistent with previous multiple-turnover studies[7]. Second, the dependence of amplitude on duplex length indicates that more protein dissociates from an